Available online at www.sciencedirect.com
ScienceDirect
ELSEVIER
Journal of Solid State Chemistry 179 (2006) 3445–3455
JOURNAL OF SOLID STATE CHEMISTRY
www.elsevier.com/locate/jssc

Stability and oxide ion conductivity in rare-earth aluminium cuspidines

M.C. Martín-Sedeño[a], D. Marrero-López[b], E.R. Losilla[a], S. Bruque[a], P. Núñez[b], M.A.G. Aranda[a,*]

[a]Departamento de Química Inorgánica, Universidad Málaga, 29071 Málaga, Spain
[b]Departamento de Química Inorgánica, Universidad La Laguna, 38200 La Laguna, Tenerife, Spain

Received 16 May 2006; received in revised form 6 July 2006; accepted 7 July 2006
Available online 21 July 2006

Abstract

$RE_4(Al_{2-x}Ge_xO_{7+x/2}\square_{1-x/2})O_2$ ($RE = Gd^{3+}$ and Nd^{3+}) oxy-cuspidine series have been prepared by ceramic method ($RE = Gd^{3+}$) and freeze-dried precursor method ($RE = Nd^{3+}$). The compositional ranges and the high temperature stability have been determined for both series. Gadolinium aluminium cuspidines are stable at very high temperatures but the analogous neodymium compounds are only stable below 1273 K. Joint Rietveld analyses of neutron powder diffraction (NPD) and laboratory X-ray powder diffraction (LXRPD) have been carried out for $Nd_4(Al_2O_7\square_1)O_2$ and $Nd_4(Al_{1.5}Ge_{0.5}O_{7.25}\square_{0.75})O_2$ compositions. Furthermore, Rietveld refinement of synchrotron X-ray powder diffraction (SXRPD) data were carried out for $Gd_4(Al_{1.0}Ge_{1.0}O_{7.5}\square_{0.5})O_2$ composition. The refinements have confirmed the known structural features of the cuspidine framework. These cuspidines series are oxide ion conductors with negligible electronic contribution as determined from impedance spectroscopy at variable oxygen partial pressures. The enhancement in the overall oxide conductivity along the two oxy-cuspidine series is two orders of magnitude. Typical ionic conductivity values for doped samples are around $4 \times 10^{-5}\,S\,cm^{-1}$ at 973 K.

Keywords: SOFC; Oxide conductor; Cuspidine; Synchrotron and neutron diffraction

1. Introduction

Solid oxide fuel cells (SOFCs) are being intensively studied as a result of the increasing interest in the development of more efficient, and environmentally friendly, ways of energy transformation [1–3]. SOFCs devices allow the direct conversion of chemical to electrical energy through an electrochemical reaction. In the SOFC technology, the electrolyte is an oxygen ion conductor of yttria-stabilised zirconia, for instance $Zr_{0.92}Y_{0.08}O_{1.96}$, (YSZ). However, the elevated operation temperatures (1073–1273 K) induces restrictions in the choice of stable materials for SOFC components which enforces the use of expensive materials with relatively low lifetimes. Therefore, there is a great need to find and develop new oxide ion conductors with improved properties at lower operation temperatures.

Most important oxide ion conductors belong principally to four different structural groups, which include the fluorite-type oxide ($Ce_{0.8}Gd_{0.2}O_{1.9}$ [4–6] and δ-Bi_2O_3 [7]), doped perovskite-type oxide (for instance: $La_{0.9}Sr_{0.1}Ga_{0.8}Mg_{0.2}O_{2.85}$ [8]), Aurivillius-type oxides (BIMEVOX, $Bi_2V_{0.86}Ni_{0.14}O_{5.29}$ [9]) and $Gd_2Ti_2O_7$ pyrochlores-derived phases [10,11]. Besides, new kinds of oxide ions conductors have been deeply studied such as oxy-apatites, for instance $La_{9.33}\square_{0.67}(SiO_4)_6O_2$ [12–16] and $La_2Mo_2O_9$-derived phases [17–21]. Nevertheless, the applicability of these materials is limited by the difficulty to obtain high density ceramics (>90%), existence of phase transition which produces a drop in conductivities values, or the low stability under reducing conditions.

As part of the attempts to discover alternative structures, a new family of oxide ion conductors derived from cuspidine structure has been recently reported [22–25]. Minerals of the cuspidine group can be described with the general formula $A_4(Si_2O_7)X_2$, where A is a large divalent cation and X is a monovalent or divalent anion (OH^-, F^-,

---

*Corresponding author. Fax: +34 952 132 000.
E-mail address: g_aranda@uma.es (M.A.G. Aranda).

0022-4596/$ - see front matter © 2006 Elsevier Inc. All rights reserved.
doi:10.1016/j.jssc.2006.07.009

O^{2-}). The archetype compound of cuspidine family is, $Ca_4(Si_2O_7)(OH)_2$ [26], which crystallises in the space group $P2_1/c$. The cuspidine framework is built up from ribbons of edge sharing CaO_7/CaO_8 polyhedra running parallel to the *a*-axis with tetrahedral disilicate groups, Si_2O_7, interconnecting theses chains through the vertexes. The structural formula of cuspidine is better described as $Ca_4(Si_2O_7\square_1)(OH)_2$ to show the empty site between disilicate group, which can be considered as an anion vacancy in the crystal structure. Several oxy-cuspidines compounds are known, such as $Eu_4(Al_2O_7\square_1)O_2$ [27], $Y_4(Al_2O_7\square_1)O_2$ [28,29], $Pr_4(Ga_2O_7\square_1)O_2$ [30] and $La_4(Ga_2O_7\square_1)O_2$ [23]. The crystal structure of $La_4(Ga_2O_7\square_1)O_2$ is shown in Fig. 1 and the positions of the oxygen vacancies have been highlighted.

The possibilities of cation substitution in the tetrahedral site for the cuspidine structure have been already studied for $RE_4(Ga_2O_9\square_1)O_2$ ($RE = La^{3+}, Nd^{3+}, Gd^{3+}$) [22–25]. These studies showed that partial aliovalent substitution of Ga^{3+} by Ge^{4+} or Ti^{4+} is accompanied by introduction of extra oxygen to charge compensation with the result of an enhancement of the oxide conductivity. In the obtained series, for instance $La_4(Ga_{2-x}Ti_xO_{7+x/2}\square_{1-x/2})O_2$ [22,25], the isolated pyrogroups transforms to infinite chains of trigonal bipyramids with some interruptions due to the oxygen vacancies. Full infinite chains of TiO_5 units are present in the end-member compound, $La_4(Ti_2O_8)O_2$. In addition, the complete electrochemical characterisation under different atmospheres revealed a significant proton contribution to the overall conductivity for Ti-doped cuspidines [25]. Finally, it must be underlined that for Ga-cuspidines, the Ge^{4+} doping leads to higher conductivity values than Ti^{4+} substitution.

Here we report the synthesis and characterisation of new oxygen ion conductors based on aluminium cuspidines, $RE_4(Al_{2-x}Ge_xO_{7+x/2}\square_{1-x/2})O_2$ ($RE = Gd^{3+}$, Nd^{3+}). Freeze-dried precursor method was used to prepare Nd-contained series, which cannot be obtained by standard ceramic route. Some members of the series have been investigated by neutron and synchrotron powder diffraction to describe the crystal structures, including the oxygen sublattice. The electrochemical characterisation has allowed establishing the main oxide conductivity features.

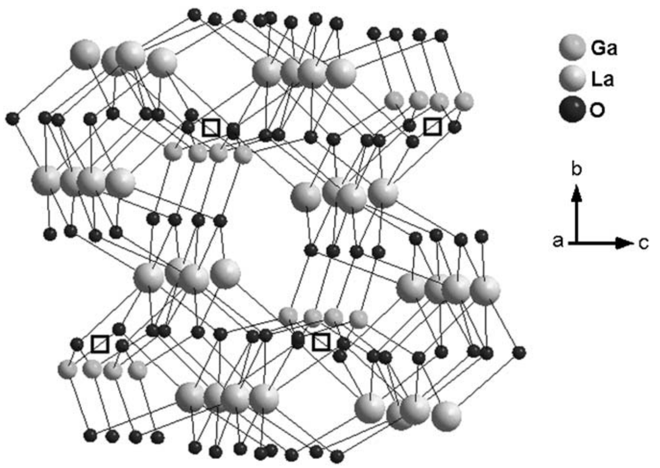

Fig. 1. Ball and stick crystal structure of $La_4(Ga_2O_7\square_1)O_2$. The positions of the oxygen vacancies ($\square$), are highlighted.

2. Experimental section

2.1. Synthesis

Two cuspidine series have been prepared: $RE_4(Al_{2-x}Ge_xO_{7+x/2}\square_{1-x/2})O_2$ ($RE = Gd^{3+}$, $x = 0.0$, 0.2, 0.4, 0.6, 0.8, 1.0, 1.2, 1.4 and 1.6; $RE = Nd^{3+}$, $x = 0.0$, 0.2, 0.4, 0.5, 0.6, 0.8 and 1.0). Gd-containing cuspidines were synthesised by conventional ceramic method using high purity oxides as starting materials: Gd_2O_3 (Alfa, 99.999%), GeO_2 (Aldrich, 99.998%) and γ-Al_2O_3 (Alfa, 99.997%). Gadolinium oxide was precalcined at 1273 K for 2 h in order to achieve decarbonation. The reagents, in stoichiometric amounts, were mixed in an agate mortar for 10 min and heated at 1373 K for 12 h. After cooling, the samples were milled for 3 h in a Fritsch ball mill (model Pulverisette 7, 45 cm^3 agate vessel containing seven agate balls with a diameter of 15 mm) at 100 rpm with reverse rotation every 20 min. The resulting powders were pelletised at 100 MPa and heated at 1673 K for 48 h in ZGS–Pt–10% Rh crucibles. $Gd_4(Al_2O_7\square_1)O_2$ needed an extra thermal treatment at 1873 K for 5 h. Pellets weight losses due to germanium volatilisation were found negligible at these temperatures and heating times. The cuspidine structure cannot be obtained by ceramic method for Nd^{3+}, a larger lanthanide ion (see Results section). Hence a second synthesis method based in freeze-dried precursor was used [19,21].

$Nd_4(Al_{2-x}Ge_xO_{7+x/2}\square_{1-x/2})O_2$ series was prepared by a freeze-dried precursor method from a stoichiometric cation solution with ethylenediamine-tetraacetic acid (EDTA) as complex agent. Neodymium oxide was dissolved in the minimum volume of nitric acid (1:1) and the pH was slowly raised up to 4 by adding ammonia. An EDTA solution 0.55 M was added under continuous stirring in a molar ratio metal/EDTA = 1/1.1 maintaining the pH between 4 and 6 with ammonia. The amorphous GeO_2 is readily soluble in water, and so, stoichiometric quantities of this compound were dissolved in the minimum volume of water, giving a solution with a final pH of ≈ 5. Then, EDTA and ammonia were added to obtain a final pH value close to 5. It is important to avoid a drastic decrease of pH values below 2 to avoid EDTA precipitation. An aqueous solution of aluminium nitrate $Al(NO_3)_3 \cdot 9H_2O$ was also prepared and the overall water content of this reagent was previously determined by thermogravimetric analysis. This solution had an initial pH$\approx$2, which was slowly raised to 4 by addition of ammonia. The complexation step of Al^{3+} ions with EDTA was done carefully maintaining the pH between 4 and 6 with ammonia under continuous stirring to avoid the precipitation of the metal hydroxide or EDTA at high or low pH values, respectively. The stoichiometric cation solutions prepared separately were mixed under constant stirring and slow heated in a hot plate to reduce the solution volume. The volume and cation concentration of the resulting solutions were ≈200 mL and 0.15 M of Nd^{3+}. Droplets of these solutions were subsequently flash frozen over liquid nitrogen and freeze-dried in a Heto Lyolab freeeze-dryer for 2 days. The dried precursor powders were calcined at 573 K for 30 min, which produces the release of a large volume of gases and a voluminous blackish powder. The resulting solids were ground in an agate mortar and heated up to the decomposition temperature (873 K for 6 h) estimated by a TGA/DTA instrument (Pyris Diamond TG/DTA, model Perkin-Elmer).

The Gd-cuspidine series prepared by the ceramic method and Nd-cuspidine prepared by freeze-dried precursor method are hereafter labelled as $GdGe_x$ and $NdGe_x$, respectively.

2.2. Powder diffraction

All samples were characterised by laboratory X-ray powder diffraction (LXRPD) at room temperature (RT). The powder patterns were collected for $NdGe_x$ series on a Siemens D5000 automated diffractometer, using graphite-monochromated $CuK\alpha_{1,2}$ radiation. The compounds were loaded in flat aluminium holders and scanned between 10° and 100° (2θ) in 0.03° steps, counting 16 s per step. High-resolution LXRPD patterns were colleted for $GdGe_x$ series in a Philips X'Pert Pro automated diffractometer, equipped with a Ge(111) primary monochromator and a X'celerator detector. The patterns were collected from 15° to 100° (2θ range) in 0.02° steps. In order to determine the thermal expansion coefficients of $NdGe_{0.2}$ and $NdGe_{0.6}$, LXRPD patterns were collected on heating each 100 K in an Anton-Paar TTK 450 camera under air conditions in the temperature range from 373 to 1073 K.

Neutron powder diffraction (NPD) patterns were collected for $NdGe_{0.0}$ and $NdGe_{0.5}$ at RT on HRPT diffractometer (SINQ neutron source at Paul Scherrer Institut, Villigen, Switzerland) with the samples loaded in vanadium cans. The wavelength ~1.886 Å, was selected by the vertically focusing Ge (511) monochromator. The overall measuring time was ~6 h per pattern to have good statistics over the 2θ angular range of 5–165° [21–0.95 Å] with 0.05° step size. Synchrotron X-ray powder diffraction (SXRPD) pattern for $GdGe_{1.0}$ was collected on ID31 diffractometer [European Synchrotron Radiation Facility (ESRF), Grenoble, France]. The sample was loaded in a borosilicate glass capillary ($\phi = 1$ mm) and rotated during data collection. A short penetrating wavelength, $\lambda = 0.40084(5)$ Å (30.9 keV), was selected with a double-crystal Si (111) monochromator and calibrated with Si standard sample from NIST ($a = 5.43094$ Å). The overall measuring time was ~1 h to have very good statistics over the angular range 2–30° (in 2θ) [11.5–0.77 Å]· The data from the multi-analyser Si (111) stage coupled with the nine scintillation detectors were normalised and summed up to 0.003° step size with local software to produce the final raw data.

Full structural characterisation was carried out for $NdGe_{0.0}$ and $NdGe_{0.5}$ by a joint Rietveld analysis of LXRPD and NPD data at RT. The structure of $GdGe_{1.0}$ has been determined from high-resolution SXRPD data because Gd has very high neutron absorption. All Rietveld [31] analyses were done using the GSAS suite of programs [32].

2.3. Microstructural characterisation

The morphology and microstructural studies of powders and sintered pellets were carried out using a JEOL SM 840 scanning electron microscope. The pellet surfaces were polished with diamond paste (12, 9, 6, 3 and 1 μm) and thermally etched at 50 K below the sintering temperature for 15 min. Finally, the samples were metallised by gold sputtering for better image definition.

2.4. Sintering conditions and conductivity measurements

Fine powders of $GdGe_x$ and $NdGe_x$ compositions were obtained by grinding the initial powdered samples in a vibratory ball mill (Retsch, 2 zircona balls with a diameter of 12.25 mm and a vessel volume of 8 cm^3) at 15 Hz for 20 min. The resulting average particle sizes were small [d_{50}~1.5–3 μm]. The particle/agglomerate size distribution was measured on a Coulter LS130 laser diffraction analyser. Electrical characterisation was carried out on cylindrical pellets (~6 mm of diameter and ~1 mm of thickness) obtained by pressing ~0.08 g of the fine powder samples at 175 MPa for 1 min. The pellets were sintered at 1773 and 1273 K for 6 h for $GdGe_x$ and $NdGe_x$ series, respectively. Electrodes were made by coating opposite pellet faces with METALOR® 6082 platinum paste and gradually heating to 1223 K at a rate of 5 K min^{-1} for 15 min in air to decompose the paste and to ensure a good conductivity and adherence. Successive treatments were made to achieve an electrical resistance lower than 1 Ω on both pellet faces.

Impedance spectroscopy data in static air were collected for $GdGe_x$ series using a Hewlett-Packard 4284A impedance analyser over the frequency range 20 Hz–1 MHz. Similar data were recorded for $NdGe_x$ series using a Solartron 1260 FRA instrument over the frequency range from 0.1 Hz to 1 MHz. The applied voltage was 200 mV in the temperature range of 1223–673 K and 250 mV between 623 and 573 K. Electrical measurements were acquired on cooling every 50 K (accuracy of ±1K) at 5 K min^{-1} and a delay time of 20 min at each selected temperature to ensure thermal stabilisation.

High-temperature conductivity measurements as a function of oxygen partial pressure [$p(O_2)$ ranges from air to ~10^{-20} atm] were performed in a closed tube furnace cell for $GdGe_{1.0}$ and $NdGe_{0.5}$ compositions. The $p(O_2)$ values were monitored by using a YSZ oxygen sensor, placed next to the pellet inside the cell. The conductivity values were continually recorded as a function of $p(O_2)$. The process consists of flushing the system with a dry 5%H_2–N_2 gas mixture for 12 h at 1173 K to reach a minimum in oxygen activity inside the furnace. After that, the oxygen partial pressure was slowly raised back to atmospheric pressure by free diffusion, because the system is not airtight. The isothermal measurement took over 72 h to complete.

3. Results and discussion

3.1. Single phase existence ranges

$Gd_4(Al_{2-x}Ge_xO_{7+x/2}\square_{1-x/2})O_2$ ($x = 0.0$, 0.2, 0.4, 0.6, 0.8, 1.0, 1.2, 1.4 and 1.6) series, $GdGe_x$, has been obtained as highly crystalline compounds by solid-state reaction. The dominant phase in our synthetic conditions is the cuspidine-type structure, although a minor crystalline phase, $GdAlO_3$ (PDF 46-0395), was identified for some samples (see Table 1). A secondary phase, Gd_2GeO_5 (PDF 78-0477), was observed for $x \geqslant 1.2$. The analysis of the LXRPD patterns by the Rietveld method showed that $GdGe_{1.2}$, $GdGe_{1.4}$ and $GdGe_{1.6}$ samples contained 1.3(2), 24.2(2) and 47.0(3) wt% of Gd_2GeO_5, respectively. Hence, the limit of the $GdGe_x$ cuspidine series must be close to $x = 1.2$ in the reported synthetic conditions.

On the other hand, all attempts to synthesise $Nd_4(Al_{2-x}Ge_xO_{7+x/2}\square_{1-x/2})O_2$ series by solid-state reaction were unsuccessful as the stable compounds at high temperatures are $NdAlO_3$ and Nd_2O_3. Fig. 2a shows the LXRPD pattern for "$Nd_4(Al_2O_7\square_1)O_2$" composition prepared at 1673 K for 48 h (ceramic method) which contains the diffraction peaks of $NdAlO_3$ and Nd_2O_3 phases and no diffraction peaks associated to the cuspidine structure were observed at temperatures between 1073 and 1673 K for $x = 0$ sample. However, cuspidine phase diffraction peaks appear as the Ge^{4+} content increases, which were linked to a decreasing of the intensities of the peaks for $NdAlO_3$ and Nd_2O_3. This behaviour demonstrates the positive effect of Al^{3+}/Ge^{4+} aliovalent substitution in the stabilisation of the cuspidine structure for these compositions. Therefore, an alternative synthesis method has been employed to obtain cuspidine phases with these stoichiometries. Synthesis of materials from precursor routes, e.g. the freeze-dried method that yields crystalline single phases at lower temperatures, is suitable to avoid the high-temperature phase segregations [19–21]. The used method starts from aqueous solutions of metals complexed with EDTA to prevent the precipitation of the hydrated oxides as described in the Experimental section. The dried powder,

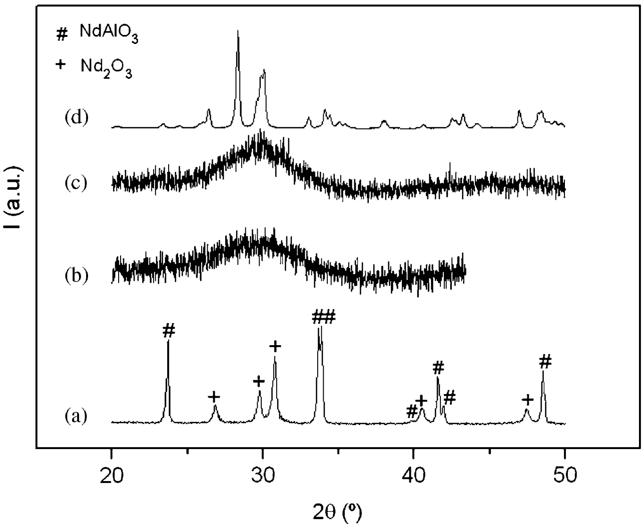

Fig. 2. LXRPD patterns of $Nd_4(Al_2O_7\square_1)O_2$ prepared from (a) solid-state reaction at 1673 K for 48 h and from freeze-dried precursor method calcined for 6 h at different temperatures: (b) 873 K, (c) 973 K and (d) 1273 K.

Table 1
Unit cell parameters and R-factors for $Gd_4(Al_{2-x}Ge_xO_{7+x/2}\square_{1-x/2})O_2$ ($x = 0.0$, 0.2, 0.4, 0.6, 0.8, 1.0 and 1.2) series from Rietveld refinements at room temperature[a]

	a (Å)	b (Å)	c (Å)	β/α (deg)	V/Z (Å^3)	R^X_{wp} (%)	R^X_F (%)	$GdAlO_3$ (%)	σ_T (S cm^{-1})
$Gd_4(Al_2O_7\square_1)O_2$[b,d]	7.5382(1)	10.6393(2)	11.2113(2)	108.989(1)	212.56(1)	2.31	6.07	0.8(1)	0.19×10^{-6}
$Gd_4(Al_{1.8}Ge_{0.2}O_{7.1}\square_{0.9})O_2$ [b,d]	7.5387(3)	10.6208(5)	11.2721(5)	109.164(3)	213.13(2)	2.19	3.42	2.5(1)	0.96×10^{-6}
$Gd_4(Al_{1.6}Ge_{0.4}O_{7.2}\square_{0.8})O_2$ [b,d]	7.5429(3)	10.6079(4)	11.3389(8)	109.465(9)	213.85(2)	2.12	3.81	0.5(1)	2.75×10^{-6}
$Gd_4(Al_{1.4}Ge_{0.6}O_{7.3}\square_{0.7})O_2$ [b,e]	10.6024(2)	10.7115(2)	3.7750(1)	89.984(8)	214.36(1)	2.37	4.59	—	7.19×10^{-6}
$Gd_4(Al_{1.2}Ge_{0.8}O_{7.4}\square_{0.6})O_2$ [b,e]	10.5872(3)	10.7272(3)	3.7748(1)	89.989(9)	214.35(1)	2.48	4.19	1.8(1)	31.6×10^{-6}
$Gd_4(Al_{1.0}Ge_{1.0}O_{7.5}\square_{0.5})O_2$[c,e]	10.5833(1)	10.7500(1)	3.7786(1)	90.000(2)	214.95(1)	2.31	3.92	0.6(1)	38.5×10^{-6}
$Gd_4(Al_{0.8}Ge_{1.2}O_{7.6}\square_{0.4})O_2$[b,e,f]	10.5741(4)	10.7681(4)	3.7748(1)	89.994(9)	214.90(2)	2.20	4.18	—	43.3×10^{-6}

The overall isothermal conductivities (at 973 K) are also given.

[a] The unit cell edges relationship for the two reported settings is given for the sake of comparison of the evolution along the series: $a(P2_1/n11) = b(P12_1/c1)$; $b(P2_1/n11)\sin\alpha = c(P12_1/c1)\sin\beta$; and $2c(P2_1/n11) = a(P12_1/c1)$.

[b] LXRPD data refinement.

[c] SXRPD data refinement at RT.

[d] Space group $P12_1/c1$.

[e] Space group $P2_1/n11$.

[f] This sample contained 1.3(2) wt% of Gd_2GeO_5.

obtained from freeze-dried, must be heated quickly at 573 K for 30 min to avoid rehydration and to start the auto-ignited process. Finally, the samples were calcined at 873 K for 6 h to obtain a light violet amorphous precursor, as revealed the LXRPD pattern (Fig. 2b for $NdGe_{0.0}$), free of carbonaceous residues because there were no appreciable mass losses above 873 K by TG. In order to follow the crystallisation process, the samples were heated for 6 h at different temperatures between 873 and 1273 K (see Figs. 2b–d). Fig. 2d shows that crystalline cuspidine-type structure is obtained at 1273 K.

In Figs. 3a and b are shown the scanning electron microscopy (SEM) images for $NdGe_{0.0}$ sample heated at 973 and 1273 K, respectively. $NdGe_{0.0}$ heated at 973 K (amorphous by LXRPD, Fig. 2c) is formed by layers of 15–20 μm of length. This compound is polycrystalline after calcined at 1273 K (Fig. 2d) and the microstructure is formed by agglomerates of small particles in the submicrometric range (Fig. 3b) with a specific surface area of ~8 $m^2\,g^{-1}$ calculated from nitrogen adsorption, using the BET method.

LXRPD data for $NdGe_x$ series indicated that the main crystalline phase for the seven members ($x = 0$–1.0) has cuspidine-type structure. A minor crystalline secondary phase, $NdAlO_3$ (PDF 76-1336), was detected in some samples (see Table 2). The analysis of the LXRPD data by the Rietveld method showed that $NdGe_{0.8}$ contained 1.9(1) and 1.3(1) wt% of Nd_2O_3 (PDF 74-2139) and $NdAlO_3$, respectively. $NdGe_{1.0}$ sample contained 1.1(1), 11.8(3), 47.5(9) and 22.9(9) wt% of Nd_2O_3, Nd_4GeO_8 (PDF 83-2423), $Nd_2Ge_2O_7$ (PDF 76-2161) and Nd_2GeO_5 (PDF 78-2406), respectively. Hence, the limit of the $NdGe_x$ cuspidine series must be close to $x = 0.8$ in the reported synthetic conditions.

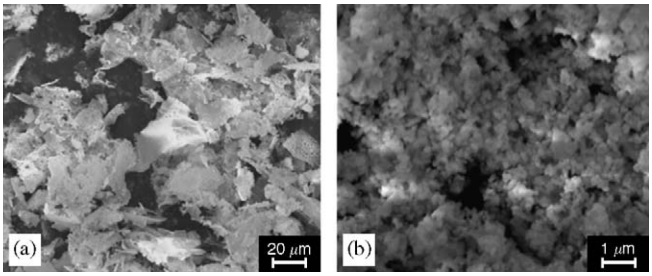

Fig. 3. SEM micrographs of $Nd_4(Al_2O_7\square_1)O_2$ sample prepared from freeze-dried precursor technique and further heated at (a) 973 K and (b) 1273 K.

The unit cell values for $GdGe_x$ and $NdGe_x$ series, determined from the Rietveld refinements of LXRPD data, are given in Tables 1 and 2, respectively. The unit cell parameters are larger for $NdGe_{0.0}$ than for $GdGe_{0.0}$, as expected based on the variation of the ionic radii of the rare-earth cations [33]. For the two series, the overall trend is a volume increasing with germanium content (Tables 1 and 2) due to the oxygen loading. However, the variation is anisotropic due to the structural features of the cuspidine-framework. Tables 1 and 2 show that a and c parameters (in the $P2_1/c$ setting) smoothly increase, and b parameter decreases, with x. This anisotropic variation is likely due to the interplay of three factors. Firstly, the introduction of extra oxygen in an empty position, to balance the charges, should expand the structure, but there is also an associate tilting of the tetrahedral groups [23] that decreases the b-parameter. Secondly, the oxygens are distributed over two available sites [23,25], which may lead to slightly different unit cell parameters. Thirdly, the sizes of Al^{3+} and Ge^{4+} are very similar but not identical. Finally, it must be underlined that the smooth variation of the unit cell parameters up to $x = 1.2$ for $GdGe_x$ (Table 1) and $x = 0.8$ for $NdGe_x$ (Table 2) confirms the formation of the solid solutions in the reported compositional ranges.

3.2. Chemical and thermal stability

The stability of the $GdGe_x$ and $NdGe_x$ cuspidine series has been studied under different temperatures, atmospheres and time. Fig. 4 show the LXRPD patterns of $NdGe_{0.0}$ and $NdGe_{0.5}$ compositions under different conditions as representative members of the series: (1) pellets for all compositions were heated at 1273 K for 24 h to investigate the thermal stability at that temperature. The samples are stable at 1273 K since they do not undergo degradation, excepting $NdGe_{0.0}$, which develops small amounts of Nd_2O_3 and $NdAlO_3$ (see Fig. 4a-left). (2) In

Table 2
Unit cell parameters and R-factors for $Nd_4(Al_{2-x}Ge_xO_{7+x/2}\square_{1-x/2})O_2$ ($x = 0.0$, 0.2, 0.4, 0.5, 0.6 and 0.8) series from Rietveld refinements at room temperature in e.g. $P12_1/c1$[a]

	a (Å)	b (Å)	c (Å)	β (deg)	V/Z (Å^3)	R^X_{wp}/R^N_{wp} (%)	R^X_F/R^N_F (%)	$NdAlO_3$ (%)	σ_T (S cm^{-1})
$Nd_4(Al_2O\square_{71})O_2$[b]	7.7402(1)	10.8543(2)	11.3083(2)	109.450(1)	223.96(1)	6.32/2.36	1.51/1.69	—	8.01×10^{-6}
$Nd_4(Al_{1.8}Ge_{0.2}O_{7.1}\square_{0.9})O_2$[c]	7.7449(3)	10.8382(4)	11.3587(4)	109.720(3)	224.38(2)	6.03/—	1.31/—	—	—
$Nd_4(Al_{1.6}Ge_{0.4}O_{7.2}\square_{0.8})O_2$[c]	7.7469(2)	10.8259(3)	11.3929(9)	109.860(9)	224.66(1)	5.88/—	1.49/—	1.2(1)	13.6×10^{-6}
$Nd_4(Al_{1.5}Ge_{0.5}O_{7.25}\square_{0.75})O_2$[b]	7.7505(1)	10.8221(2)	11.4030(5)	109.878(6)	224.86(1)	6.10/3.59	2.14/2.96	1.6(1)	25.4×10^{-6}
$Nd_4(Al_{1.4}Ge_{0.6}O_{7.3}\square_{0.7})O_2$[c]	7.7563(2)	10.8147(4)	11.4118(5)	109.931(5)	224.98(2)	6.24/—	2.65/—	1.4(1)	36.5×10^{-6}
$Nd_4(Al_{1.2}Ge_{0.8}O_{7.4}\square_{0.6})O_2$[c]	7.7629(3)	10.8122(5)	11.4155(7)	109.814(7)	225.35(2)	8.71/—	2.10/—	1.3(1)	44.3×10^{-6}

The overall isothermal conductivities (at 973 K) are also given.

[a] All atoms are located at the general position: 4e, Wyckoff notation.

[b] Joint LXRPD and NPD data refinement at RT.

[c] LXRPD data refinement.

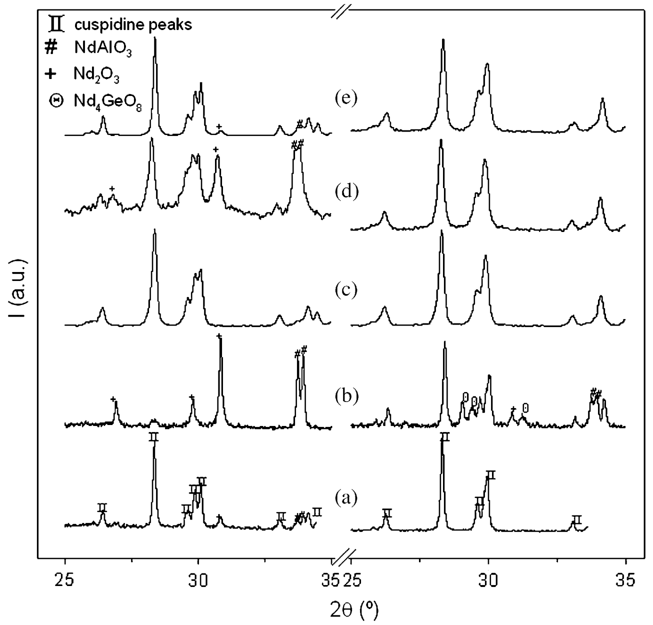

Fig. 4. LXRPD patterns for $Nd_4(Al_2O_7\Box_1)O_2$ (left) and $Nd_4(Al_{1.5}Ge_{0.5}O_{7.25}\Box_{0.75})O_2$ (right) of the pristine compounds treated under different conditions: (a) heated at 1273 K for 24 h; (b) heated at 1373 K for 6 h; (c) heated at 1073 K for 24 h under a flow of 5%H_2–N_2; (d) heated at 1073 K for 50 h under a flow of 5%H_2–N_2; (e) heated at 1173 K for 24 h under a flow of 5%H_2–N_2.

addition, all samples were heated at 1373 K for 6 h to evaluate the possible degradation at higher temperature. The powder diffraction studies revealed total decomposition of the cuspidine structure to $NdAlO_3$ and Nd_2O_3 for $NdGe_{0.0}$ (see Fig. 4b-left). It must be underlined that the phase segregation decreases with increasing germanium content (see Fig. 4b-right), leading also to Nd_4GeO_8 as side-phase. (3) Furthermore, the pristine samples were heated at 1073 and 1173 K under reducing conditions, constant flow of 5%H_2–N_2. LXRPD patterns for $NdGe_{0.0}$ indicated that the phase is stable at 1073 K for 24 h (Fig. 4c-left) but it decomposes into $NdAlO_3$ and Nd_2O_3 after 50 h at the same temperature (Fig. 4d-left). A thermal treatment at 1173 K for 24 h, under identical conditions, revealed the presence of minor amounts of $NdAlO_3$ and Nd_2O_3 (Fig. 4e-left). Conversely, $NdGe_{0.5}$ is stable under reducing atmosphere at 1073 and 1173 K for 50 h (Figs. 4c–e-right). (4) A last test was made to study the stability of these phases under moisture conditions. $NdGe_{0.0}$ was heated at 1123 K under a constant flux of $\approx$3% H_2O–air. The LXRPD pattern of the resulting sample (not shown) indicated a partial decomposition into $NdAlO_3$ and Nd_2O_3. A similar treatment for $NdGe_{0.8}$ did not show evidences of decomposition. All results showed above indicate that the Al^{3+}/Ge^{4+} aliovalent substitution increase the stability of the cuspidine structure for $RE = Nd^{3+}$. Finally, it must be highlighted that $GdGe_x$ series does not undergo decomposition under the conditions described above. This behaviour clearly indicates that aluminium cuspidines present higher stability with smaller rare-earth cations like Gd^{3+}.

3.3. Crystal structures

A joint refinement of NPD and LXRPD data for $Nd_4(Al_2O_7\Box_1)O_2$ and $Nd_4(Al_{1.5}Ge_{0.5}O_{7.25}\Box_{0.75})O_2$ were carried out at RT in $P2_1/c$ space group as previously described for $La_4(Ga_{2-x}Ge_xO_{7+x/2}\Box_{1-x/2})O_2$ [23] and $La_4(Ga_{2-x}Ti_xO_{7+x/2}\Box_{1-x/2})O_2$ [25] cuspidine series. The neutron wavelength was refined in the simultaneous analysis of $Nd_4(Al_2O_7\Box_1)O_2$ and it converged to 1.88551(6) Å. This value was used in all subsequent Rietveld analyses. The occupation factors of O(5) and O(10), which join the trigonal bypiramid chains [23,25], were freely refined given 0.52(4) and 0.81(4), respectively. The occupation factors of the two Al/Ge sites were also refined but constrained to full occupancy of each site. The refined structural stoichiometry for $NdGe_{0.5}$ was $Nd_4(Al_{1.45(8)}Ge_{0.55(8)}O_{7.33(8)})O_2$ which is in good agreement with the nominal stoichiometry, $Nd_4(Al_{1.5}Ge_{0.5}O_{7.25})O_2$. The temperature factors of O(5) and O(10) were constrained to be the same to avoid correlations in the refinements. The final fits were very good for both compositions and the refined atomic parameters are given in Table 3. Bond distances and selected bond angles are given in the supplementary material in Tables S1 and S2. The Rietveld fits of the neutron and X-ray data for $NdGe_{0.5}$ sample are shown in Fig. 5.

The insertion of oxygen into the vacant position, O(10), and the partial emptying of O(5) in the $NdGe_x$ series equalise the two different distances initially present in the dialuminate groups and between them, respectively. So, the isolated tetrahedral dialuminate present in $Nd_4(Al_2O_7\Box_1)O_2$ are converted to infinite bipyramid chains with some interruptions due to partial occupancy of both oxygens in $Nd_4(Al_{1.5}Ge_{0.5}O_{7.25}\Box_{0.75})O_2$ (see Fig. 6). The observed trend in the Al–O bond distances is fully consistent with the previous findings for the Ga–O distances, also obtained by NPD, in related doped cuspidines [23,25].

The crystal structure of $Gd_4(Al_{1.0}Ge_{1.0}O_{7.5}\Box_{0.5})O_2$ at RT has been described from SXRPD data using the structure of $La_4(Ga_{1.0}Ti_{1.0}O_{7.5}\Box_{0.5})O_2$ as starting model in the non-standard monoclinic space group $P2_1/n11$. NPD data were not acquired due to the high absorption of the Gadolinium cations. The absence of neutron data does not allow to describe the structure in $P2_1/c$ space group and hence, an approximate (simplified) structure is described in $P2_1/n11$ with half-unit cell. The occupation factors of Al(1) and Ge(1) were fixed to their nominal values and they were refined later. The occupation factor of O(3) was fixed to its nominal value and it was not refined. The temperature factors of O(1), O(2), O(4) and O(5) were constrained to be the same to avoid correlations in the refinements. The synchrotron pattern showed anisotropic broadening with asymmetric tails for some reflections, which is likely linked

Table 3
Positional parameters for $Gd_4(Al_{1.0}Ge_{1.0}O_{7.5}\square_{0.5})O_2$ in e.g. $P2_1/n11$[a], $Nd_4(Al_2O_7\square_1)O_2$ and $Nd_4(Al_{1.5}Ge_{0.5}O_{7.25}\square_{0.75})O_2$ in e.g. $P12_1/c1$[b] at RT

	$GdGe_{1.0}$[c]				$NdGe_{0.0}$[d]				$NdGe_{0.5}$[d]			
Atom	x	y	z	U_{iso} (Å^2)	x	y	z	U_{iso} (Å^2)	x	y	z	U_{iso} (Å^2)
$RE(1)$	0.1258(1)	0.0726(1)	0.2501(9)	0.009(1)	0.5251(4)	0.0989(2)	0.7906(2)	0.004(1)	0.524(1)	0.095(1)	0.794(1)	0.014(2)
$RE(2)$	0.4020(1)	0.2080(1)	0.7455(9)	0.014(1)	0.0262(4)	0.0860(2)	0.8099(2)	0.004(1)	0.027(1)	0.088(1)	0.802(1)	0.004(2)
$RE(3)$	—	—	—	—	0.3347(5)	0.1255(3)	0.4276(3)	0.003(1)	0.338(1)	0.125(1)	0.421(1)	0.002(2)
$RE(4)$	—	—	—	—	0.8362(5)	0.1235(3)	0.4166(3)	0.003(1)	0.843(1)	0.127(1)	0.429(1)	0.007(2)
$M(1)$[e]	0.1793(3)	0.3774(3)	0.2894(9)	0.011(1)	0.2198(9)	0.1942(9)	0.1283(8)	0.007(3)	0.198(4)	0.189(2)	0.125(2)	0.036(8)
$M(2)$[e]	—	—	—	—	0.6527(9)	0.1856(9)	0.1171(8)	0.006(3)	0.652(2)	0.190(2)	0.122(2)	−0.001(7)
O(1)	0.0037(8)	0.1064(9)	0.7133(9)	0.004(2)	0.7802(9)	0.2204(8)	0.7470(6)	0.010(2)	0.768(3)	0.223(2)	0.754(2)	0.023(6)
O(2)	0.2696(9)	0.0279(9)	0.8305(9)	0.004(2)	0.2368(8)	0.2247(7)	0.7642(6)	0.002(2)	0.242(3)	0.218(2)	0.761(2)	0.013(5)
O(3)[f]	0.2303(9)	0.3851(9)	0.6707(9)	−0.006(5)	0.2114(9)	0.0366(9)	0.1668(8)	0.018(2)	0.201(2)	0.042(1)	0.176(1)	0.001(4)
O(4)	0.2723(9)	0.2355(9)	0.2805(9)	0.004(2)	0.0834(9)	0.2357(7)	0.9805(6)	0.009(2)	0.138(2)	0.233(2)	0.973(2)	0.010(4)
O(5)[g]	0.0228(9)	0.3369(9)	0.2012(9)	0.004(2)	0.4362(9)	0.2386(5)	0.1173(6)	0.009(1)	0.425(6)	0.221(2)	0.112(2)	0.012(3)
O(6)	—	—	—	—	0.6355(9)	0.2291(7)	0.9658(6)	0.010(2)	0.628(3)	0.230(2)	0.968(2)	0.016(5)
O(7)	—	—	—	—	0.7052(9)	0.0365(8)	0.1711(7)	0.007(2)	0.713(3)	0.034(2)	0.162(1)	0.012(5)
O(8)	—	—	—	—	0.0757(9)	−0.0001(7)	0.3937(9)	0.001(1)	0.079(3)	0.006(2)	0.397(1)	0.001(4)
O(9)	—	—	—	—	0.5658(9)	0.0051(7)	0.3969(9)	0.008(2)	0.561(3)	0.001(2)	0.396(2)	0.006(4)
O(10)[g]	—	—	—	—	—	—	—	—	0.052(3)	0.744(1)	0.373(2)	0.012(3)

[a] All atoms are located at the general position 4c, Wyckoff notation.

[b] All atoms are located at the general position 4e, Wyckoff notation.

[c] SXRPD data refinement.

[d] Joint LXRPD and NPD refinement.

[e] M = Al/Ge with occupation factors: Al(1) = 0.46 (1), Ge(1) = 0.54 for $GdGe_{1.0}$ and Al(1) = 0.63(4), Ge(1) = 0.37, Al(2) = 0.82(4), Ge(2) = 0.18 for $NdGe_{0.5}$.

[f] Nominal occupation factors for O(3) is 0.75 for $GdGe_{1.0}$.

[g] Occupation factors for O(5) and O(10) are 0.52(4) and 0.81(4), respectively, for $NdGe_{0.5}$.

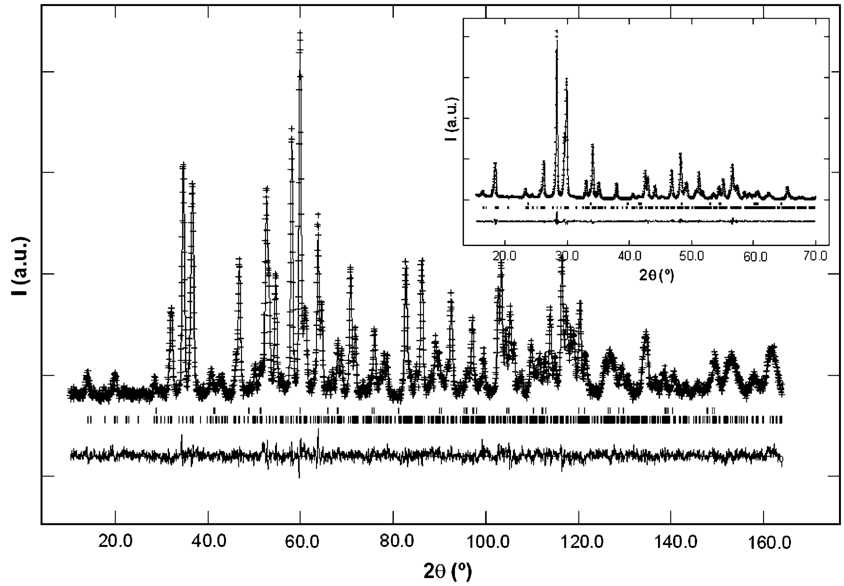

Fig. 5. Observed (crosses), calculated (full line) and difference (bottom) NPD Rietveld patterns ($\lambda = 1.89$ Å) for $Nd_4(Al_{1.5}Ge_{0.5}O_{7.25}\square_{0.75})O_2$ at RT. The vertical bars are the allowed Bragg reflections. The inset shows a selected region (15–70°/2θ) of the LXRPD Rietveld patterns ($\lambda = 1.54$ Å) for the same composition.

to the morphology of the crystallites plus some lack of oxygen ordering in the crystals, which has recently been pointed out [24]. The final refined atomic parameters are given in Table 3 and bond distances and selected bond angles are given in the supplementary material in Tables S1 and S2. The Rietveld plot of the synchrotron X-ray data is displayed in Fig. 7.

The volume thermal expansion coefficient for $NdGe_{0.2}$ and $NdGe_{0.6}$ samples, derived from high-resolution LXRPD data taken each 100 K, was $\alpha_v = 16.0(4) \times 10^{-6}$

and $20.2(7)\times10^{-6}\,K^{-1}$, respectively [$\alpha_v$ is defined as m/n for the $V(T)=n+mT(K)$ linear fitting]. Under the isotropic thermal expansion approximation, the linear expansion coefficient, β_{calc}, can be derived as $\beta_{calc}=\alpha_v/3$ being $5.3(1)\times10^{-6}$ and $6.7(2)\times10^{-6}\,K^{-1}$ for $NdGe_{0.2}$ and $NdGe_{0.6}$, respectively.

3.4. Sintering conditions and impedance study

The sintering conditions for the pellets of $GdGe_x$ series at 1773 K led to dense specimens with compactions ranging between 96% and 99% of the theoretical value (taking into account the pellets mass, volume and the crystallographic density). Fig. 8a shows a SEM micrograph for $GdGe_{1.0}$ sintered pellet, showing the microstructure with average grain size ranging between 1 and 2 μm and low porosity. However, it can be observed that some grains are not well interconnected. No indications of liquid phase formation or phase segregations at the grain boundary were found in any studied samples. Additionally, no contamination due to the ball-milling process was detected in the sintered pellets. On the other hand, the limited thermal stability range for $NdGe_x$ series resulted in porous samples. The pellets density values are ~65%, at the highest possible sintering temperature 1273 K, which are low for an accurate measurements of ionic conductivities. Successive grinds were carried out in a vibratory ball mill for 20 min at 15 Hz to improve the compactions at 1273 K without success. Fig. 8b shows a SEM micrograph for $NdGe_{0.5}$ sintered pellet, where large pores are observed. The porosity makes difficult to estimate the corresponding

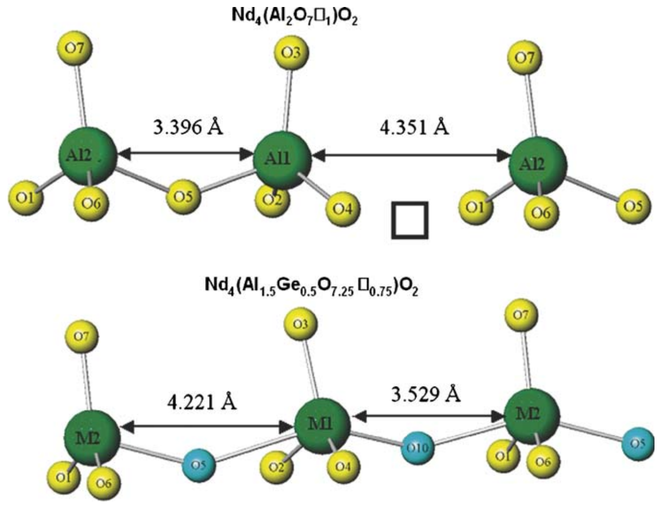

Fig. 6. Ball and stick view of (bottom) tetrahedral condensed digallate groups for $Nd_4(Al_2O_7)O_2$ showing the vacant oxide site; (top) distorted trigonal-bipyramid gallate chains for $Nd_4(Al_{1.5}Ge_{0.5}O_{7.25}\square_{0.75})O_2$ highlighting the O(5) and O(10) partial occupied sites.

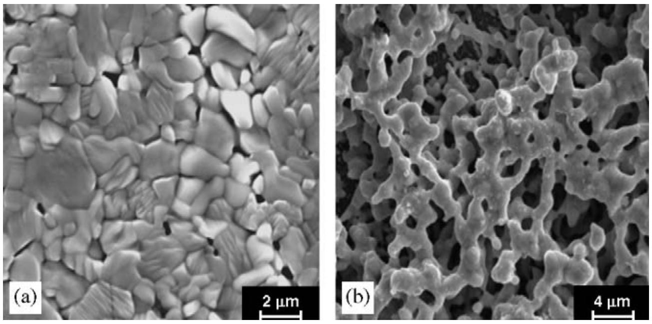

Fig. 8. SEM micrographs of polished and thermally etched surfaces of the sintered pellets for (a) $Gd_4(Al_{1.0}Ge_{1.0}O_{7.5}\square_{0.5})O_2$ and (b) $Nd_4(Al_{1.5}Ge_{0.5}O_{7.25}\square_{0.75})O_2$.

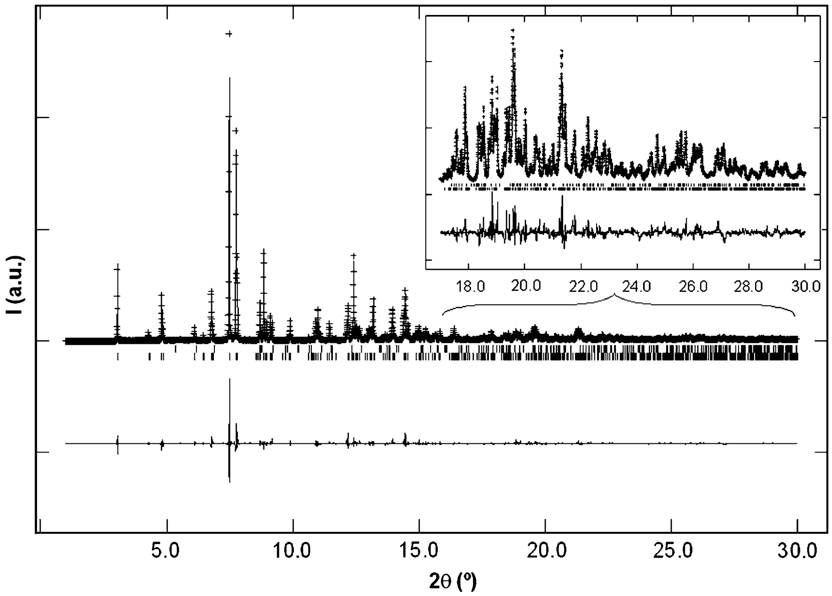

Fig. 7. Observed (crosses), calculated (full line) and difference (bottom) RT-SXRPD patterns ($\lambda = 0.40$ Å) for $Gd_4(Al_{1.0}Ge_{1.0}O_{7.5}\square_{0.5})O_2$. The vertical bars are the allowed Bragg reflections. The inset shows an enlarged view of the high angle region.

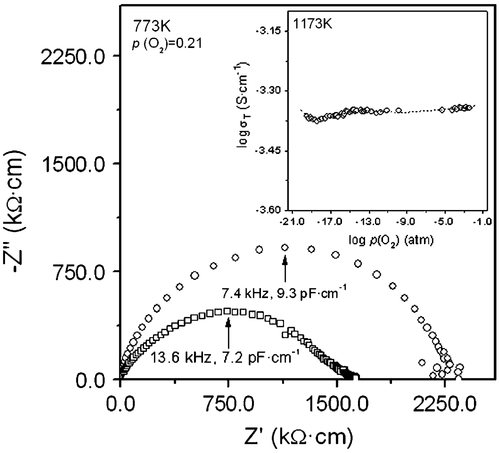

Fig. 9. Complex impedance spectra for $Gd_4(Al_{1.0}Ge_{1.0}O_{7.5}\square_{0.5})O_2$ (○) and $Nd_4(Al_{1.5}Ge_{0.5}O_{7.25}\square_{0.75})O_2$ (□) at 773 K in air. Frequencies and capacitances are highlighted for selected frequency data. The inset shows overall conductivity at 1173 K as a function of oxygen partial pressure for $Gd_4Ge_{1.0}$ sample. The dashed line is a guide to the eyes.

grain sizes, although the material has good connectivity between the microparticles.

Representative impedance data for one composition of each series, $GdGe_{1.0}$ and $NdGe_{0.5}$, at 773 K are shown as impedance complex plane plots in Fig. 9; similar plots were obtained for all compositions. For $GdGe_{1.0}$, an almost non-deformed semicircle is observed with an associated capacitance at the maximum of 9.3 pF cm^{-1}. For $NdGe_{0.5}$, a set of overlapped semicircles can be observed. This set of semicircles indicates that at least two different contributions due to grain interior (bulk) and internal interfaces (grain boundary and porosity) are present. Lower frequency processes are observed at high temperature in the form of a well-developed spike, with an associated capacitance of 0.031 μF cm^{-1} at 20 Hz and 1173 K for $GdGe_{1.0}$ (not shown). From these data, it may be concluded that the samples show principally ionic conductivity as previously reported for related cuspidine materials [22–25].

To investigate the electrical microstructure of the pellets is useful to analyse the spectroscopic plots ($-Z''/M''$ vs. log*f*) for the same impedance data since it allows determining whether the overall pellet resistances represent the bulk resistance of the grains or were influenced by grain boundary effects. Spectroscopic plots for $GdGe_{1.0}$ (Fig. 10a) have the maxima of both curves quite close (less than one order of magnitude in frequency) which indicates that the impedance peak is associated with the same RC element responsible of the modulus peak, however the associated capacitances (8.4 pF cm^{-1} for M'' and 9.3 pF cm^{-1} for Z'') are somewhat larger than those expected for a homogeneous bulk value (~2 pF cm^{-1} is expected assuming a typical high-frequency permittivity ε' of 10–20). Furthermore, the M'' peak shows a shoulder at high frequencies that corresponds to a more conductive element. This relaxation is not well defined at low temperatures because the data dispersion likely due to the high electrical resistance of the material. To further examine this point, we have plotted the real part of the complex capacitance as a function of frequency (not shown). At low frequencies, the blocking electrode effect can be observed and, at higher frequencies, the curves show a clear relaxation from ~9 pF toward lower values in the pF range as frequency increases. The relaxation at ~9 pF is attributed to a very thick grain boundary or constriction resistance at the region of grain–grain contacts that may be observed in the SEM micrograph (Fig. 8a). This component dominates the Z'' spectrum and represents the main part of the total resistance of the samples.

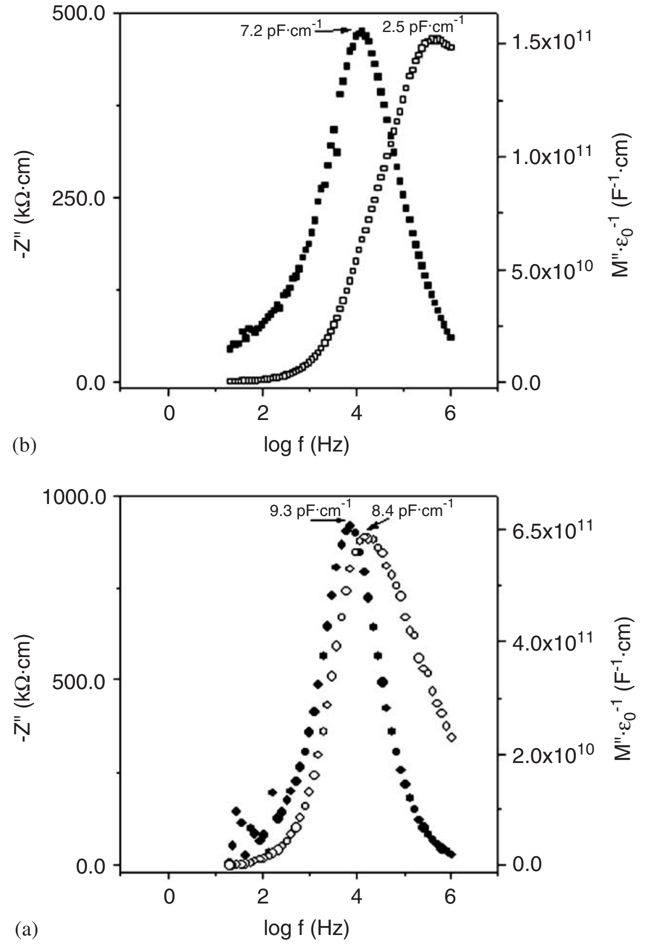

Fig. 10. Spectroscopic plots at 773 K of $-Z''$ (close points) and M'' (open points) vs. log*f* for (a) $Gd_4(Al_{1.0}Ge_{1.0}O_{7.5}\square_{0.5})O_2$ (circles) and (b) $Nd_4(Al_{1.5}Ge_{0.5}O_{7.25}\square_{0.75})O_2$ (squares).

Spectroscopic plots for $NdGe_{0.5}$ show a large separation between the two maxima of almost two orders of magnitude in frequency (Fig. 10b). The associated capacitance to the M'' maximum (2.5 pF cm^{-1}) is bulk characteristic, meanwhile the associated capacitance of the Z'' maximum (7.2 pF cm^{-1}) can be ascribed to a grain boundary contribution. The Z'' peak is not symmetric and an overlapped shoulder is observed at high frequencies close to the maximum of the M'' peak. It must be noted that the grains in $NdGe_{0.5}$ are well interconnected, as

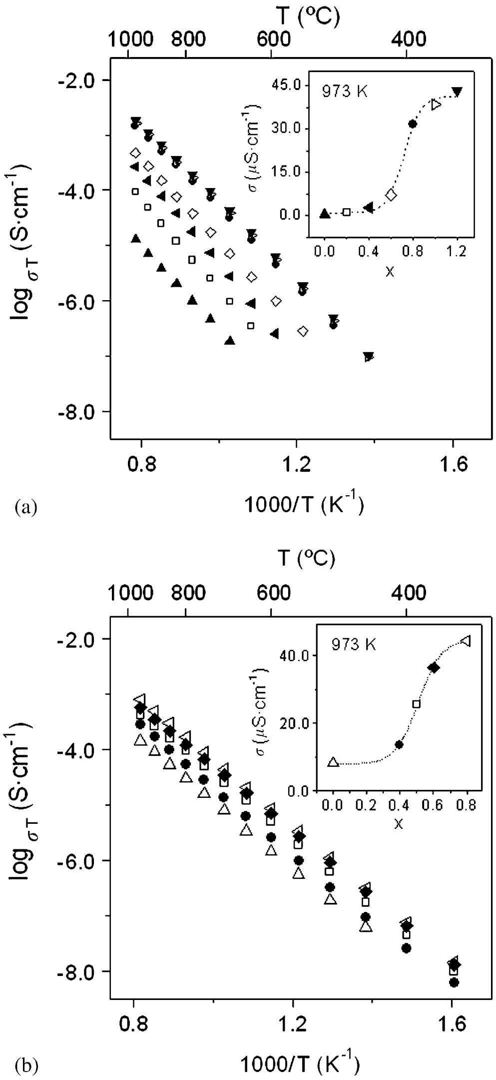

Fig. 11. Arrhenius plots of $\log \sigma_T$ for (a) $Gd_4(Al_{2-x}Ge_xO_{7+x/2}\square_{1-x/2})O_2$ $(0.0 \leqslant x \leqslant 1.2)$ series and (b) $Nd_4(Al_{2-x}Ge_xO_{7+x/2}\square_{1-x/2})O_2$ $(0.0 \leqslant x \leqslant 0.8)$ series. The insets show the variation of the overall conductivity as function of Ge content at 973 K, the dashed line is a guide to the eyes.

revealed by the SEM micrograph (Fig. 8b), which allows the oxide migration through the pellet.

Overall pellet conductivities (σ_T) are obtained from the intercept of the spikes and/or the arcs (low frequency ends) on the Z'-axis, and are given in Figs. 11a and b in the traditional Arrhenius representation. These plots of overall conductivities fall on a set of straight lines without large discontinuities between compositions. For $GdGe_x$ series (Fig. 11a), the calculated activation energies range between 1.49(1) and 1.40(1) eV for $GdGe_{0.0}$ and $GdGe_{1.2}$, respectively. For $NdGe_x$ series (Fig. 11b), the activation energies values are very close to 1.19(1) eV for all compositions. The small spreading of these values suggests that the oxide conductivity mechanism does not change along the series. Intermediate activation energies, 1.2–1.3 eV, have been reported for $Nd_4(Ga_{2-x}Ge_xO_{7+x/2}\square_{1-x/2})O_2$ and $Nd_4(Ga_{2-x}Ti_xO_{7+x/2}\square_{1-x/2})O_2$ series [24].

The variation of total conductivity with Ge-content (at 973 K) under static air for $GdGe_x$ and $NdGe_x$ series, are given in the insets of Fig. 11. These values increase with Ge content, likely reaching a maximum for the highest Germanium-loaded materials, $GdGe_{1.2}$ and $NdGe_{0.8}$ compositions. The conductivity values for $GdGe_x$ and $NdGe_x$ series at 973 K are given in Tables 1 and 2, respectively. These conductivity values are slightly lower than those previously reported for the $Nd_4(Ga_{2-x}Ge_xO_{7+x/2}\square_{1-x/2})O_2$ series [24] at the same temperature: 3.7×10^{-5} S cm^{-1} for $Nd_4(Ga_{1.6}Ge_{0.4}O_{7.2}\square_{0.8})O_2$. However, the values are not directly comparable because the high porosity of the $NdGe_x$ samples. Furthermore, cuspidine materials with a large cation, i.e. Ga^{3+}, at the tetrahedral site seems to display higher conductivity values compared to those derived from smaller cations like Al^{3+}. The lower volume cell for $Nd_4(Al_2O_7\square)O_2$ (223.96 Å^3) compared to $Nd_4(Ga_2O_7\square)O_2$ (231.5 Å^3) probably reduce the free space for oxygen diffusion and consequently the conductivity decreases.

The ionic conductivity is independent of the oxygen partial pressure, $p(O_2)$, for a pure ionic conductor. However, the conductivity increases for a mixed ionic–electronic conductor as $p(O_2)$ increases or decreases, depending on the predominant electronic contribution (p- and n-type, respectively). The conductivity data for $GdGe_{1.0}$ at 1173 K as a function of $p(O_2)$ are shown in the inset of Fig. 9. As it can be observed, the conductivity is almost independent of oxygen partial pressure, which suggests pure oxide-ion conduction with negligible electronic contribution within the studied oxygen partial pressure range. In addition, the conductivity of $NdGe_{0.5}$, which is stable under a constant flow of 5%H_2–Ar at 1073 K, was also studied as function of $p(O_2)$, and it also remains constant.

4. Conclusions

Two cuspidine series, $RE_4(Al_{2-x}Ge_xO_{7+x/2}\square_{1-x/2})O_2$ ($RE = Gd^{3+}$ and Nd^{3+}), have been prepared as solid solutions up to $x = 1.2$ for Gd^{3+} and 0.8 for Nd^{3+}. The Gd-containing series could be prepared by ceramic method at high temperature, 1673 K, but the Nd-containing phases are not stable at high temperatures and cannot been prepared by standard solid-state reaction route. The Nd series was prepared at much lower temperatures, 1273 K, from freeze-dried precursor method. Neutron and synchrotron powder diffraction data have confirmed the known structural features of the cuspidine framework. The enhancement in the overall oxide conductivity along the two oxy-cuspidine series is two orders of magnitude with negligible electronic contribution. However, the reported oxide conductivity values are somewhat smaller than those previously reported for similar doped oxy-cuspidine-containing Ga^{3+} cations.

Acknowledgments

Financial support from the MAT2003-7483-C2-1 and MAT2004-3856 research grants is acknowledged. ESRF is thanked for the provision of X-ray synchrotron facilities. This work was partially performed at the spallation neutron source SINQ, Paul Scherrer Institut, Villigen, Switzerland. We thank Dr. Sheptyakov (SINQ) and Dr. Brunelli (ESRF) for help during the neutron and synchrotron experiments, respectively.

Appendix A. Supplementary data

Supplementary data associated with this article can be found in the online version at doi:10.1016/j.jssc.2006.07.009.

References

[1] R.M. Ormerod, Chem. Soc. Rev. 32 (2003) 17.

[2] A.B. Stambouli, E. Traversa, Renew. Sustain. Energy Rev. 6 (2002) 433.

[3] B.C.H. Steele, A. Heinzel, Nature 414 (2001) 345.

[4] H. Inaba, H. Tagawa, Solid State Ion. 83 (1996) 1.

[5] K.Q. Huang, M. Feng, J.B. Goodenough, J. Am. Ceram. Soc. 81 (1998) 357.

[6] D.P. Fagg, J.C.C. Abrantes, D. Pérez-Coll, P. Núñez, V.V. Kharton, J.R. Frade, Electrochim. Acta 48 (2003) 1023.

[7] T. Takahashi, H. Iwahara, Y. Nagai, J. Electrochem. Soc. 117 (1970) 244.

[8] T. Ishihara, H. Matsuda, Y. Takita, J. Am. Chem. Soc. 116 (1994) 3801.

[9] F. Krok, I. Abrahama, D. Bango, W. Bogusz, J.A.G. Nelstrop, Solid State Ion. 111 (1998) 37.

[10] S.A. Kramer, H.L. Tuller, Solid State Ion. 82 (1995) 15.

[11] H.L. Tuller, Solid State Ion. 94 (1997) 63.

[12] S. Nakayama, T. Kageyama, H. Aono, Y. Sadaoka, J. Mater. Chem. 5 (1995) 1801.

[13] M.S. Islam, J.R. Tolchard, P.R. Slater, Chem. Commun. (2003) 1486; J.R. Tolchard, M.S. Islam, P.R. Slater, J. Mater. Chem. 13 (2003) 1956.

[14] L. León-Reina, M.C. Martín-Sedeño, E.R. Losilla, A. Cabeza, M. Martínez-Lara, S. Bruque, F.M.B. Marques, D.V. Sheptyakov, M.A.G. Aranda, Chem. Mater. 15 (2003) 2099.

[15] L. León-Reina, E.R. Losilla, M. Martínez-Lara, S. Bruque, M.A.G. Aranda, J. Mater. Chem. 14 (2004) 1142.

[16] L. León-Reina, E.R. Losilla, M. Martínez-Lara, S. Bruque, A. Llobet, D.V. Sheptyakov, M.A.G. Aranda, J. Mater. Chem. 15 (2005) 2489.

[17] P. Lacorre, F. Goutenoire, O. Bohnke, R. Retoux, Y. Laligant, Nature 404 (2000) 856.

[18] J.A. Collado, M.A.G. Aranda, A. Cabeza, P. Olivera-Pastor, S. Bruque, J. Solid State Chem. 167 (2002) 80.

[19] D. Marrero-Lopez, J. Canales-Vázquez, J.C. Ruiz-Morales, J.T.S. Irvine, P. Núñez, Solid State Ion. 176 (2005) 1807.

[20] D. Marrero-López, J.C. Ruiz-Morales, D. Pérez-Coll, P. Nuñez, J.C.C. Abrantes, J.R. Frade, J. Solid State Electrochem. 8 (2004) 638.

[21] D. Marrero-López, J. Canales-Váquez, J.C. Ruiz-Morales, J.T.S. Irvine, P. Núñez, Electrochim. Acta 50 (2005) 4385.

[22] O. Joubert, A. Magrez, A. Chesnaud, M.T. Caldes, V. Jayaraman, Y. Piffard, L. Brohan, Solid State Sci. 4 (2002) 1413.

[23] M.C. Martín-Sedeño, E.R. Losilla, L. León-Reina, S. Bruque, D. Marrero-López, P. Núñez, M.A.G. Aranda, Chem. Mater. 16 (2004) 4960.

[24] A. Chesnaud, O. Joubert, M.T. Caldes, S. Gosh, Y. Piffard, L. Brohan, Chem. Mater. 16 (2004) 5372.

[25] M.C. Martín-Sedeño, D. Marrero-López, E.R. Losilla, L. León-Reina, S. Bruque, P. Núñez, M.A.G. Aranda, Chem. Mater. 17 (2005) 5989.

[26] S. Saburi, A. Kawahara, C. Henmi, I. Kusachi, K. Kihara, Mineral. J. 8 (1977) 286.

[27] C.D. Brandle, H. Steinfink, Inorg. Chem. 8 (1969) 1320.

[28] A.N. Christensen, R.G. Hazell, Acta Chem. Scand. 45 (1991) 226.

[29] H. Yamane, M. Shimada, B.A. Hunter, J. Solid State Chem. 141 (1998) 466.

[30] Th.M. Gesing, R. Uecker, J.C. Buhl, Z. Kristallogr. 214 (1999) 431.

[31] H.M. Rietveld, J. Appl. Crystallogr. 2 (1969) 65.

[32] A.C. Larson, R.B. von Dreele, GSAS program, Los Alamos National Laboratory Report No. LA-UR-86748, 1994.

[33] R.D. Shannon, Acta Crystallogr. A 32 (1976) 751.